


RESEARCH ARTICLE

Sea ice heat and mass balance measurements from four autonomous buoys during the MOSAiC drift campaign

Don Perovich^{1,*} , Ian Raphael¹, Ryleigh Moore², David Clemens-Sewall¹, Ruibo Lei³, Anne Sledd^{4,5}, and Chris Polashenski¹

As part of the Multidisciplinary drifting Observatory for the Study of Arctic Climate (MOSAiC), four autonomous seasonal ice mass balance buoys were deployed in first- and second-year ice. These buoys measured position, barometric pressure, snow depth, ice thickness, ice growth, surface melt, bottom melt, and vertical profiles of temperature from the air, through the snow and ice, and into the upper ocean. Observed air temperatures were similar at all four sites; however, snow-ice interface temperatures varied by as much as 10°C, primarily due to differences in snow depth. Observed winter ice growth rates (November to May) were <1 cm day⁻¹, with summer melt rates (June to July) as large as 5 cm day⁻¹. Air temperatures changed as much as 2°C hour⁻¹ but were dampened to <0.3°C hour⁻¹ at the snow-ice interface. Initial October ice thicknesses ranged from 0.3 m in first-year ice to 1.2 m in second-year ice. By February, this range was only 1.20–1.46 m, due in part to differences in the onset of basal freezing. In second-year ice, this delay was due to large brine-filled voids in the ice; propagating the cold front through this ice required freezing the brine. Mass balance results were similar to those measured by autonomous buoys deployed at the North Pole from 2000 to 2013. Winter average estimates of the ocean heat flux ranged from 0 to 3 W m⁻², with a large increase in June 2020 as the floe moved into warmer water. Estimates of average snow thermal conductivity measured at two buoys during periods of linear temperature profiles were 0.41 and 0.42 W m⁻¹ °C⁻¹, higher than previously published estimates. Results from these ice mass balance buoys can contribute to efforts to close the MOSAiC heat budget.

Keywords: Sea ice, Mass balance, Heat fluxes

1. Introduction

There has been a dramatic reduction in Arctic sea ice in recent decades. Ice extent has been decreasing in all months, particularly in September (Stroeve et al., 2012, 2014; Meier et al., 2014, 2021). The ice cover has shifted from one dominated by older, more resilient ice to a younger, more fragile sea ice cover (Maslanik et al., 2011; Tschudi et al., 2016; Kwok, 2018; Kwok et al., 2019). The thermodynamic sea ice mass balance is simply the amount of ice grown in the winter minus the amount melted on

the ice surface and bottom during summer. Sea ice mass balance measurements provide insights into the causes of Arctic sea ice loss. They can help to delineate between the impacts of snow depth, ice thickness, the surface heat budget, and the ocean heat flux (Perovich et al., 2014; Perovich and Richter-Menge, 2015; Lei et al., 2018; Planck et al., 2020).

The recent decline in Arctic sea ice motivated the Multidisciplinary drifting Observatory for the Study of Arctic Climate (MOSAiC) project, a large international, interdisciplinary project. Its overarching science question is “What are the causes and consequences of a diminished Arctic sea ice cover?” The centerpiece of MOSAiC was a yearlong drift experiment in the Central Arctic (Nicolaus et al., 2022). Manual and autonomous mass balance measurements were made throughout the MOSAiC field experiment (Lei et al., 2022; Nicolaus et al., 2022).

In addition to the primary Central Observatory (CO) of the MOSAiC field campaign, an extended network of measurement sites called the Distributed Network was established to explore spatial variability (Krumpfen et al., 2020; Rabe et al., n.d.). One element of the Distributed Network

¹ Thayer School of Engineering, Dartmouth College, Hanover, NH, USA

² Department of Mathematics, University of Utah, Salt Lake City, UT, USA

³ Key Laboratory for Polar Science of the MNR, Polar Research Institute of China, Shanghai, China

⁴ Cooperative Institute for Research in Environmental Sciences, CU Boulder, Boulder, CO, USA

⁵ NOAA Physical Sciences Laboratory, Boulder, CO, USA

* Corresponding author:

Email: donald.k.perovich@dartmouth.edu

was a triangular array of autonomous instruments spaced tens of kilometers from the CO. We deployed three autonomous seasonal ice mass balance buoys (SIMBs; Planck et al., 2019) as part of the Distributed Network, with a fourth buoy deployed at the CO. The SIMBs measure geographic location, barometric pressure, snow depth, ice thickness, ice growth, surface melt, bottom melt, and vertical temperature profiles through the snow and ice.

Here we report the seasonal evolution of snow depth, ice thickness, ice growth rates, onset dates of melt and freezeup, and vertical profiles of temperature in the snow and ice obtained from the four SIMBs. Similarities and differences between the four sites are discussed. A detailed analysis of results from the longest-lasting buoy provides summer melt rates, temporally averaged estimates of the ocean heat flux, and effective thermal conductivity of the snow. These observations provide insights into the relative contributions of atmospheric and oceanic forcing to the observed decline in Arctic sea ice.

2. Methods

Four SIMBs were deployed during October 2019 at the beginning of the MOSAiC field experiment. One was deployed at “Met City” in the CO. The other three were deployed at the three “L” sites as part of the MOSAiC Distributed Network (Rabe et al., n.d.). At L1, L2, and L3, the SIMBs were co-located with other autonomous instruments observing the atmosphere, sea ice, and ocean. The L site ice floes were selected to (i) sample a variety of different ice conditions and (ii) form a roughly equilateral triangle surrounding the MOSAiC Central Observatory at a distance of tens of kilometers. The four SIMBs are referred to as CO, L1, L2, and L3.

The SIMBs deployed at MOSAiC were spar buoys designed to float upright in open water (Polashenski et al., 2011; Planck et al., 2019). The buoy is a cylinder of ABS plumbing pipe covered in white vinyl shrink wrap that is 4.87 m long and 0.117 m in diameter. The buoy power supply is designed for a 2-year life expectancy. The instrument package consisted of a downward-facing acoustic rangefinder positioned above the ice that measured surface position, an upward-looking acoustic rangefinder positioned underneath the ice that measured ice bottom position, a vertical digital temperature chain, and air temperature and barometric pressure sensors (**Figure 1**). The digital temperature chain had 192 elements placed at 0.02 m spacing and extended from the air through the snow, through the ice, and into the upper ocean. It is the same chain installed on the SIMBA buoys (Lei et al., 2022). However, in the SIMBs the temperature chain is mounted directly on the pipe and the heating elements of the chain are not used. All measurements were collected every 4 hours and transmitted through the Iridium satellite network.

For each SIMB, the initial measurements of snow depth and ice thickness were made at installation. The time series of air temperature, barometric pressure, snow depth, ice thickness, and snow and ice temperature were transmitted and posted on a website in real time. All data are archived at the Arctic Data Center (Perovich et al.,

2022). Snow accumulation and loss were determined, as were ice growth and surface and bottom melt. Snow and ice melt was converted into meltwater production. Temperature profiles were used to calculate the heat content and temperature gradient of the snow and sea ice layers. Results were also used to calculate time-averaged estimates of the ocean heat flux to the ice and the effective thermal conductivity of snow. The details of these calculations are presented in Section 3.

3. Results

3.1. General mass balance

The drift track of MOSAiC is shown in **Figure 2** along with the layout of the buoys at deployment. The drift was from the Eastern Arctic north toward the North Pole and then south along the Transpolar Drift Current. Ice motion was extremely fast (Belter et al., 2021; Krumpfen et al., 2021) and the MOSAiC CO reached the marginal ice zone at the end of July 2020. The average ice velocity was 0.15 m s^{-1} . The largest monthly displacement of the buoys was in March 2020, when they moved 350 km from 82.3°N , 34.15°E to 85.2°N , 15.97°E .

MOSAiC was located in a very dynamic region with a mixture of first-year and second-year ice, which impacted the working duration of the SIMBs. All four buoys were deployed in October 2019, with the buoys lasting from 4 months to 10 months (**Table 1**). Initial ice thickness at installation ranged from 0.30 m to 1.20 m. The L3 buoy was installed in first-year ice, and the CO, L1, and L2 buoys were in second-year ice. The L3 SIMB was crushed in a pressure ridge on February 3, 2020, and L1 was crushed on March 15, 2020. An ice dynamics event encased the lower portion of the CO buoy in ice blocks on December 3, 2019. However, the buoy was not destroyed and continued to function until May 14, 2020, at which point it was crushed by ice dynamics. The L2 buoy lasted until the MOSAiC floe broke up in late July 2020 (Nicolaus et al., 2022).

Maximum observed ice thicknesses were 1.32 m (L3), 1.78 m (L1), and 1.90 m (L2), though the maximum thicknesses observed at L1 and L3 were not true maxima as they were destroyed before the end of the growth season in mid-May. After being embedded in a ridge, the acoustic sensor was not able to measure the thickness at the CO buoy. Maximum snow depth varied by nearly a factor of four from 0.14 m on the first-year ice of L3 to 0.54 m on the deformed ice of CO. There were snow drifts at the CO site due to local ridges and built structures. A transect survey over the CO and around the MOSAiC floe revealed that the ridge surface accumulated on average nearly five times the snow depth as level ice by the beginning of April, when the snow depth reached its annual maximum (Itkin et al., 2023). This range in snow depth implies that the SIMB deployment sites can approximately represent both the snow on ice ridges and snow on level ice.

The time series of air temperatures and snow–ice interface temperatures at the four buoys are compared in **Figure 3**. Air temperatures were quite similar at the four buoys, with variations of only a degree or two. There were large differences of up to 10°C in the snow–ice interface temperatures. Snow–ice interface temperature differences

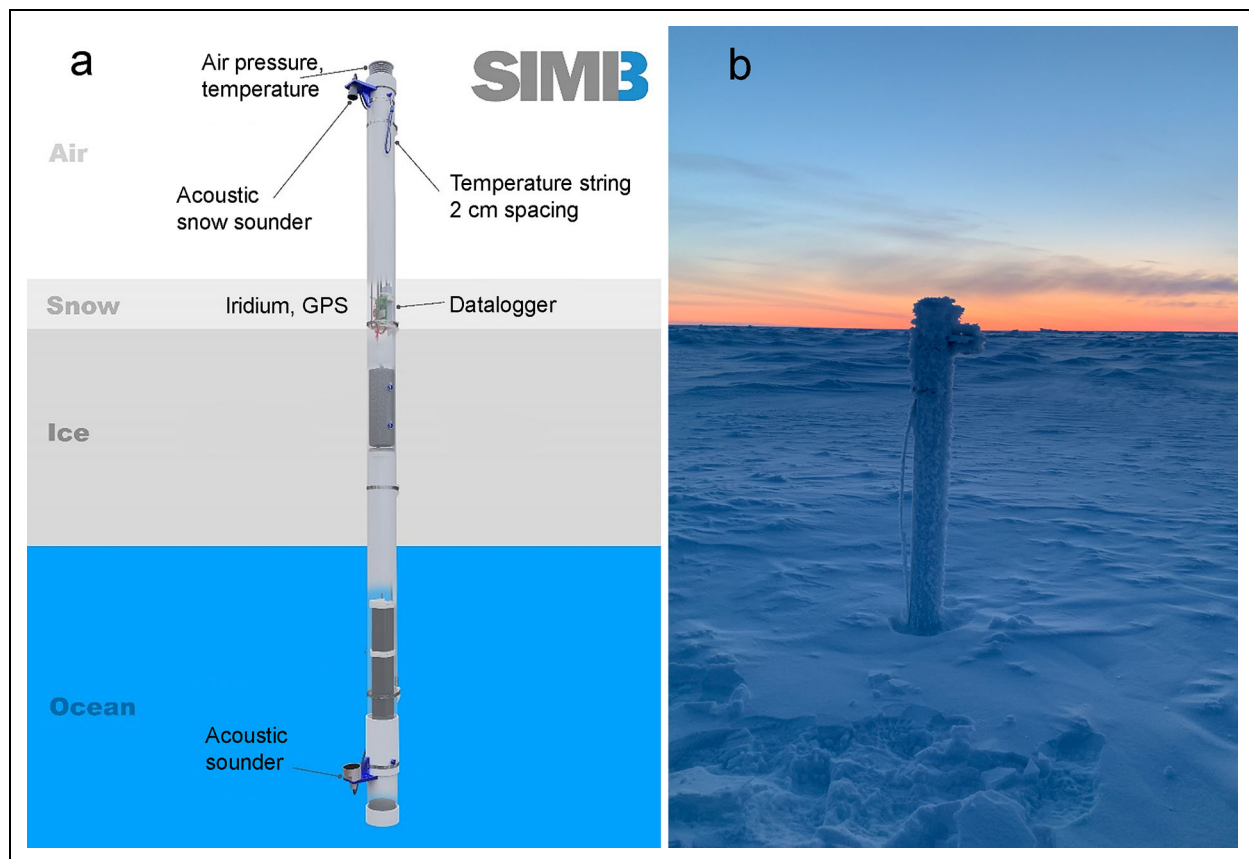


Figure 1. The seasonal ice mass balance (SIMB) buoy. (a) Schematic of the SIMB buoy and (b) photograph of the SIMB buoy installed at L1 site. Photograph courtesy of Anne Gold.

were only a few degrees from October into December, when the variability began to increase, reaching a maximum in early March. Variations in snow–ice interface temperature can result from differences in snow depth and ice thickness. As the winter progressed, the ice thickness differences between sites decreased and snow depth differences increased. The increase in snow depth variability resulted from blowing snow forming drifts near ridges. Thus, the increased variability in snow–ice interface temperature at these sites was likely due to increased differences in snow depth among the sites. After a December ridging event at the CO buoy, a snow drift formed around the buoy resulting in much deeper snow (>0.4 m) than at the other sites. Interface temperatures at the CO were consistently 5–10°C warmer than the other sites throughout the winter until air temperatures warmed in April, illustrating the impact of snow as a thermal insulator.

The time series of ice mass balance and temperature of the four sites are shown in **Figure 4**. In early fall, the cold temperatures gradually propagate down toward the ice bottom. The cold front reaches the bottom faster in thin ice than in thicker ice. For example, ice growth had already begun at installation for the 0.30 m thick ice at the L3 site and started a few days after installation at the 0.43 m thick ice at the CO. In contrast, at the 1.20 m thick L1 site, there was still melting at the ice bottom just after installation and growth did not start until mid-December. Bottom growth at L1 was delayed by large voids of brine in

the ice. The impact of the delay on ice growth and slower growth rates are evident comparing ice growth for L1 and L3 from installation to February 1, 2020. L3 had 1.00 m of growth from 0.30 m to 1.30 m compared to only 0.26 m of growth from 1.20 m to 1.46 m at L1. The thinner ice almost “caught up” to the ice that initially was 0.9 m thicker.

On January 14, 2020, there was a rapid increase in ice thickness at L2 from 1.33 m to 1.46 m (**Figure 4c**). This increase was not due to thermodynamic growth, but rather to the accumulation of platelet ice. The platelet ice was assimilated into basal ice growth at L2 by February 10, 2020. Katlein et al. (2020) reported extensive platelet ice formation at the MOSAiC CO (Nicolaus et al., 2022) from January 2020 until the end of March 2020. Results from L2 show that platelet ice extended tens of kilometers beyond the CO. Mass balance buoy data also indicate that while platelet ice was widespread, there was also small scale variability in platelet ice accumulation. At the L3 floe, our mass balance buoy found no platelet ice at our site, while there was platelet ice at a buoy reported in Lei et al. (2022).

The propagation of air temperature into the ice is evident in the color contours of **Figure 4**. The dark blue (cold) temperature contours are intermittent and only propagate 0.2 m to 0.3 m into the ice. Occasionally temperatures propagated deeper into the ice during an air temperature change of longer duration, such as the warm

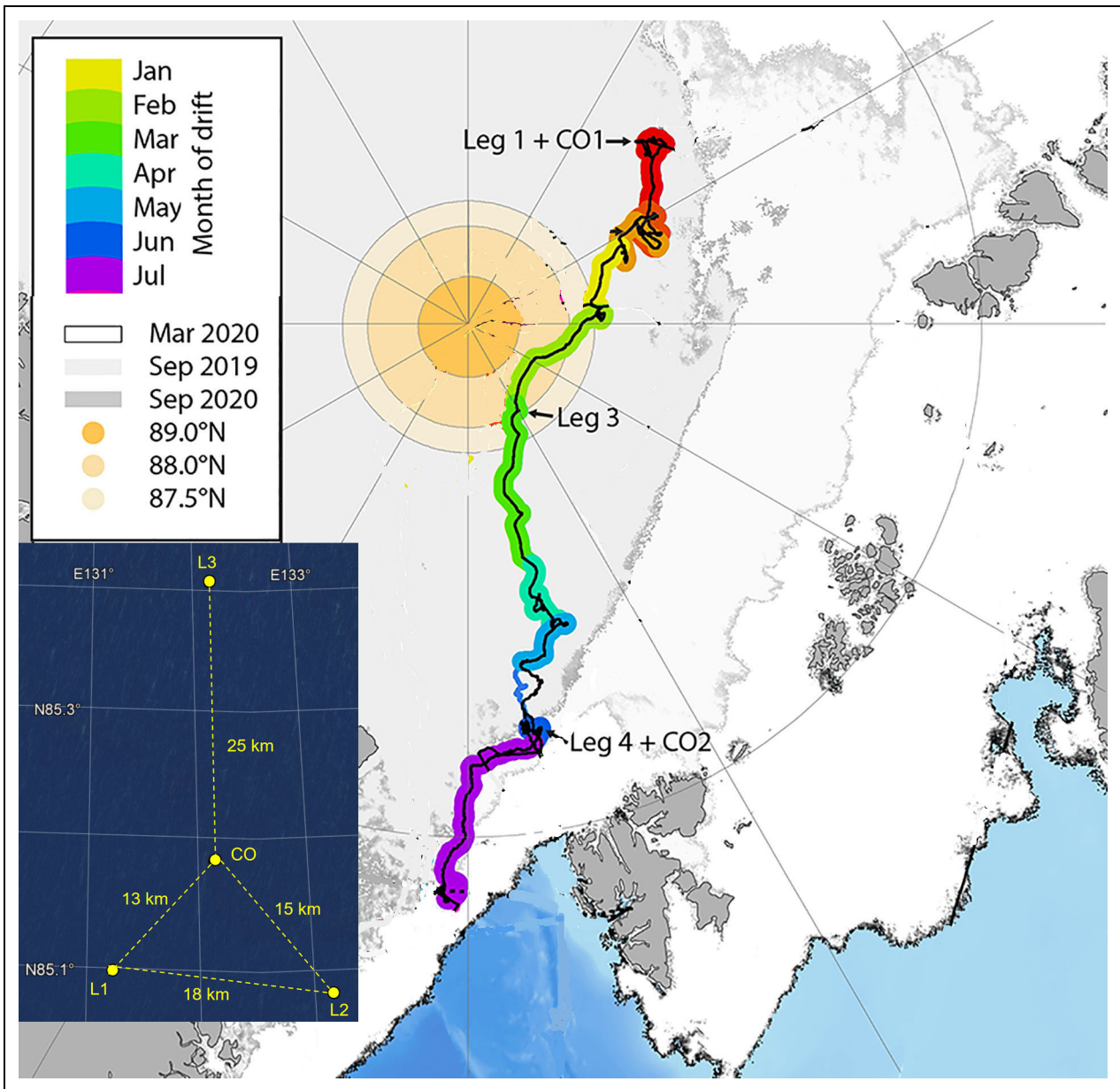


Figure 2. Drift track of MOSAiC. The drift track of the MOSAiC and the ice extent in September 2019, March 2020, and September 2020. The Central Observatory (CO) included an initial floe (CO1) until Leg 4 when a second CO (CO2) was established. L1, L2, and L3 denote three remote sites deployed during MOSAiC. This figure is a modified version of figure 1 in Nicolaus et al. (2022). The insert shows the layout of the four seasonal ice mass balance buoys (the CO buoy and L1, L2, and L3) on October 21, 2019.

period from November 10 to November 17 when air temperatures increased from -32°C to -5°C (red/yellow increase). Temperature changes lower in the ice are due to seasonal trends in air temperature, rather than synoptic events. Deeper snow further insulates the ice from changes in air temperature. Due to snow accumulation in February at the CO site, ice temperatures never dropped below -16°C after February, even as the coldest ice temperatures of the year occurred at the other sites.

3.2. Ridge consolidation at the CO

The ice thickness and temperature evolution of the CO SIMB was different from the other sites. In December and January, there was a considerable amount of ridging

around the CO buoy. The CO buoy was embedded in, but not destroyed by, a ridge in early December. An ice block likely obscured the under-ice acoustic sensor ending direct measurements of ice thickness. At the same time, the ice temperature contours became much steeper than the other sites, complicating estimation of ice thickness from temperature profiles. The cooling was much faster than the other sites, and much faster than can be explained by conduction through the ice and snow. This difference is possibly due to some ice blocks collecting around the temperature chain when the sea ice was deformed. These cold ice blocks would freeze the seawater next to the buoy, thus accelerating the decrease in temperature.

Table 1. Summary of results on snow depth, ice thickness, and melt from the four seasonal ice mass balance buoys

Parameter	Seasonal Ice Mass Balance Buoy			
	L1	L2	L3	CO
Ice type	Second year	Second year	First year	Second year
Start (in 2019)	Oct 5, 07:00	Oct 7, 00:24	Oct 10, 08:01	Oct 21, 08:01
Latitude	85.01	85.00	85.13	85.10
Longitude	132.75	134.96	135.43	132.64
End (in 2020)	Mar 15, 23:03	Jul 30, 2:39	Feb 3, 12:07	May 14, 6:01
Latitude	86.84	79.60	87.59	83.39
Longitude	15.01	−1.66	91.26	9.88
Maximum snow depth (m)	0.24	0.24	0.14	0.54
Start of ice growth (in 2019)	Dec 17	Nov 10	Oct 10 ^a	Oct 28
Initial ice thickness (m)	1.20	0.80	0.30	0.43
Maximum ice thickness (m)	1.78	1.90	1.32	— ^b
Total surface melt, snow + ice (m)	—	0.39	—	—
Total surface melt, ice (m)	—	0.31	—	—
Total bottom melt (m)	—	0.30	—	—
Total ice growth (m)	0.58	1.10	1.02	—
Start, surface snow melt	—	Jun 8, 2020	—	—
Start, surface ice melt	—	Jun 29, 2020	—	—
Start, bottom melt	—	Jun 11, 2020	—	—

^aBottom growth was occurring at L3 at installation.

^bNot available.

The temperature chain, which is fastened to the hull of the SIMB, remained vertical as shown in **Figure 5**, an important point when analyzing the temperature results. The temperature chain is fragile; if it had detached from the hull it would have failed. If it remained attached to the hull and the hull broke, the entire buoy would have failed. The continued operation of the buoy indicates that the temperature chain was not disturbed by the nearby ridging.

Figure 6 allows a closer look at CO ice temperatures from December through January by showing the time series from sensors spaced at 0.1 m intervals from 1 m to 2.7 m below the surface of the ice. A group of temperature sensors all drop below -2°C between January 2 and January 5, 2020 (**Figure 6a**), showing an increase in freezing front depth from 1.6 m to 2.5 m in only 3 days. The freezing front is denoted by the temperature dropping below -2°C . There is a steady progression of the freezing front for the second half of December (**Figure 6c**). However, the average growth rate is 3.8 cm day^{-1} , much faster than thermodynamic ice growth. The ice growth observed at L1, L2, and L3 is also plotted in **Figure 4** contour plots and in **Figure 6b**, demonstrating that the passage of the freezing front at the CO site was not due to bottom ice growth.

Vertical temperature profiles at selected times are plotted in **Figure 6b**. The December 2, 2019, profile is a typical

undeformed ice temperature profile: constant temperature in the air, nearly linear gradients in the snow and ice, a larger gradient in the snow than ice, and water temperatures at the freezing point below the ice. The profile on January 13, 2020, is much different. The freezing front is at a depth of 2.64 m compared to 0.74 m on December 2, 2019. This increase of 1.90 m is far too large for normal thermodynamic growth. The bottom portion of the profile is also unusual in being below the freezing point and nearly vertical, suggesting that the buoy is in ice. The rapid increase of the freezing front suggests a process other than vertical conduction through the ice causing the cooling.

3.3. Summer melt

The L2 buoy had the longest lifetime, lasting from October to July, and was the only SIMB to survive into the summer melt season. L2 results are first used to determine surface and bottom melt and then the amount of meltwater produced. Surface and bottom melt were determined from the above ice and below ice acoustic sensors. The top panel in **Figure 7** shows the 3-day running average of surface and bottom melt rates at L2 from the onset of melt in early June to July 12. Melt rates were averaged to smooth uncertainties in the acoustic sounder measurements. Snow melt rates are reported as ice equivalents, scaled by $330\text{ kg m}^{-3}/900\text{ kg m}^{-3}$. Surface melt started on

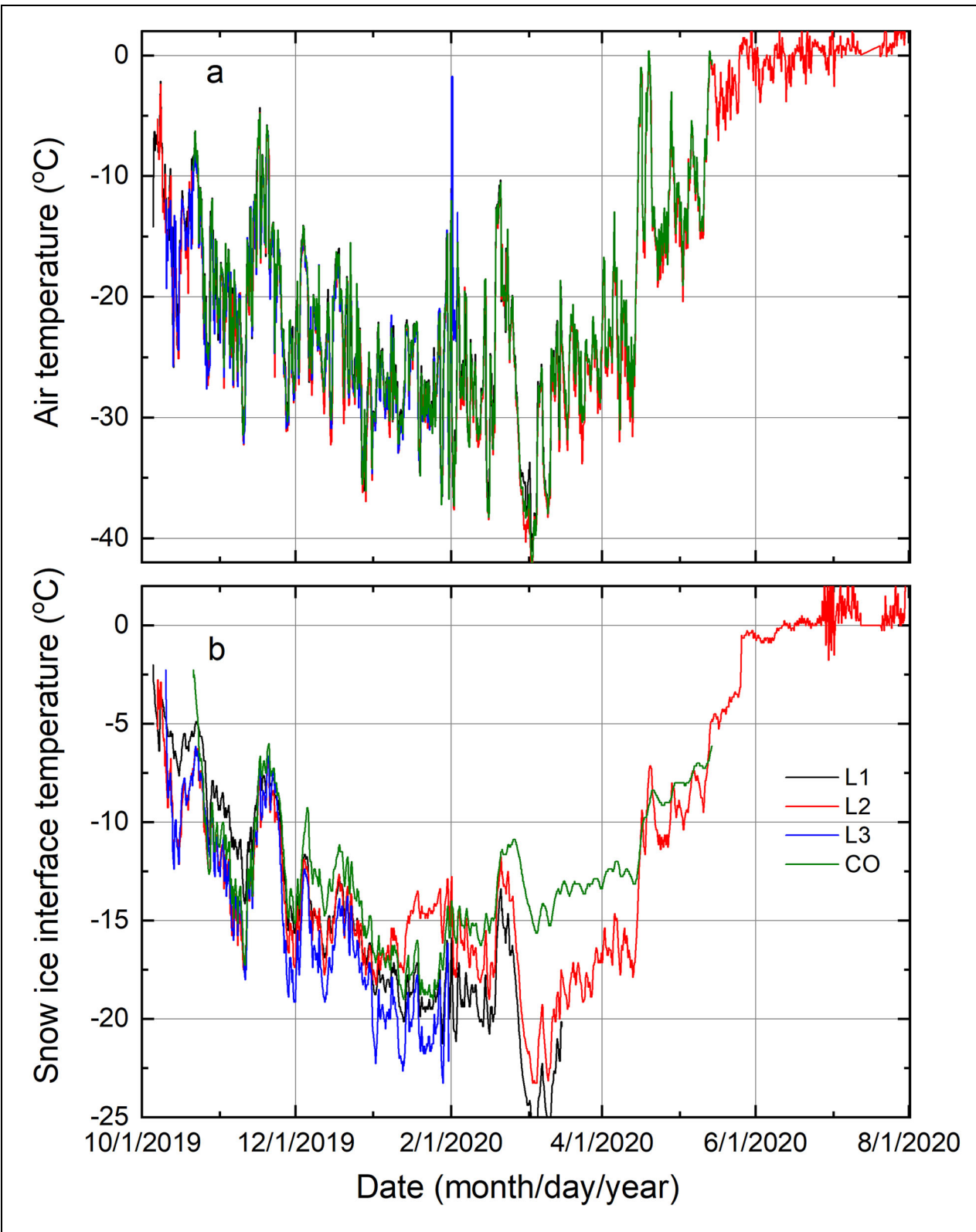


Figure 3. Time series of air and snow–ice interface temperatures. Time series of (a) air temperature and (b) snow–ice interface temperature for the four, color-coded seasonal ice mass balance buoys (L1, L2, L3, and CO).

June 8 and bottom melt began on June 11. On June 29, surface melt transitioned from snow to ice. In total there was 0.20 m of snow melt, equivalent to 0.07 m of ice melt, 0.32 m of surface ice melt, and 0.27 m of bottom ice melt.

Figure 7b shows the daily ice equivalent meltwater input from both snow and ice melt. From June 8 to June

22, meltwater produced by bottom melt was greater than surface melt due primarily to surface melt being snow. Surface melt was then larger for the remainder of the observation period. The bottom panel shows the cumulative meltwater input. By July 12, there was a total of 0.25 m of meltwater produced by bottom melt and 0.35 m

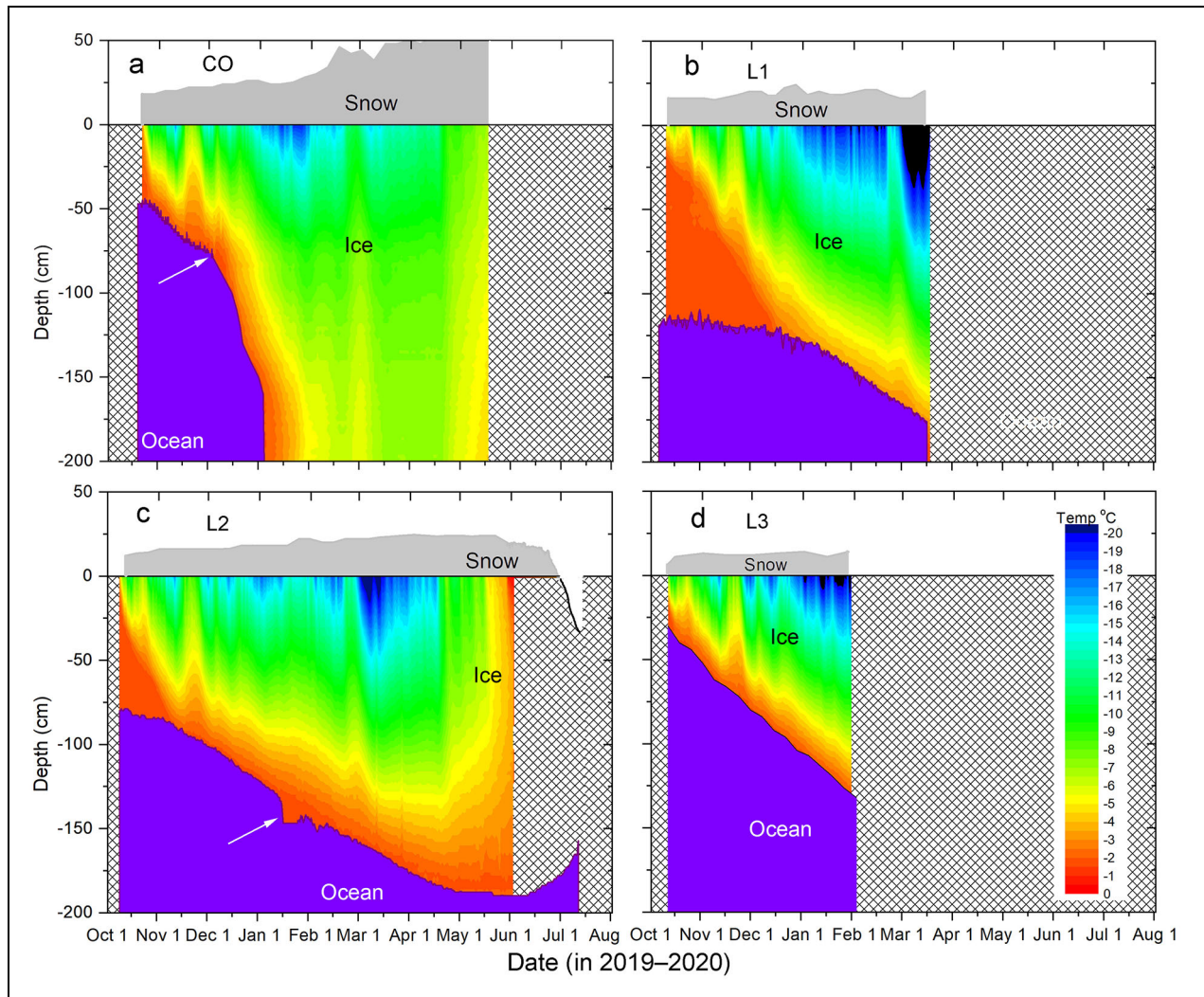


Figure 4. Mass balance plots for the four seasonal ice mass balance buoys. Data are derived from the seasonal ice mass balance buoys: (a) CO, (b) L1, (c) L2, and (d) L3. Color contours represent temperatures in the ice. The gray-shaded area is snow. The purple area is the ocean. The hatched area indicates missing data. The arrow in (a) shows when the under-ice acoustic sensor failed. Ice bottom positions after this point were determined from temperature profiles. The arrow in (c) highlights the deposition of platelet ice.

from surface melt. This meltwater contributed to the formation of meltwater layers in the upper ocean directly under the ice and to false bottoms (Smith et al., 2022).

3.4. Ocean heat flux

The ocean heat flux can be determined from measurements of the vertical eddy flux of sensible heat (McPhee, 1992; Maykut and McPhee, 1995; Krishfield and Perovich, 2005). This effort entails measuring time series of vertical profiles of ocean temperature, salinity, and current, as well as determining the ice bottom roughness. Temporally averaged values of F_w can also be determined from relatively simple measurements of ice temperature and mass balance (McPhee and Untersteiner, 1982; Wettlaufer, 1991; Perovich and Elder, 2002).

As first presented by MCPhee and Untersteiner (1982), ice temperature profiles and ablation or growth at the ice bottom can be used to calculate the ocean heat flux by

treating it as a residual of the conductive (Q_f), specific (Q_s), and latent (Q_L) heats of the ice.

$$F_w = \left(\frac{1}{\Delta t} \right) (Q_f + Q_s + Q_L). \quad (1)$$

Cooling, freezing, and upward heat flow are negative, and warming, melting, and downward heat flux are positive. The details of this approach are presented in MCPhee and Untersteiner (1982). For these calculations, we assumed that the thermal conductivity of ice was $2 \text{ W m}^{-1} \text{ }^\circ\text{C}^{-1}$ and that the salinity in the lower portion of the ice was 3.

The primary uncertainty in this approach is determining the amount of ice growth or melt at the bottom. The acoustic sensors have an uncertainty of $\pm 0.5 \text{ cm}$. This indirect approach works best when averaging over long time intervals. Uncertainties in ocean heat flux resulting from uncertainties in changes at the ice bottom are about 20 W m^{-2} for daily estimates, 3 W m^{-2} for weekly



Figure 5. Photograph of the Central Observatory seasonal ice mass balance buoy. The red arrow points to the seasonal ice mass balance buoy (circled). Ridges can be seen near the buoy. The photograph was taken on May 4, 2020, by Martin Radenz.

estimates, 1.5 W m^{-2} for biweekly estimates, and 0.6 W m^{-2} for monthly estimates. Because of these uncertainties, ocean heat fluxes calculated over periods of days to a week tend to be noisy.

Results from the L2 buoy (**Figure 4c**) were used to calculate estimates of the ocean heat flux (F_w). Issues with the other three buoys precluded their use in this analysis. The CO buoy was embedded in a ridge, the L1 had large void spaces filled with brine, and L3 failed in January. The platelet ice that accumulated at L2 complicated the analysis. For example, considering platelet ice to be ice growth, the ocean heat flux calculated from January 10 to January 24, 2020, is -16 W m^{-2} . This calculation is incorrect, however, as platelet ice is not a solid slab of ice, but rather a loose, aggregated collection of ice plates. We tempered the impact of platelet ice by applying a linear fit to the bottom position from January 13, 2020, before the start of platelet formation, to February 10, 2020, after the end of a distinct platelet layer.

Biweekly averages of ocean heat flux at L2 are presented in **Figure 8** along with an 8th order polynomial fit to the data ($R^2 = 0.97$). The ocean heat flux in early November was 11 W m^{-2} . This flux is likely due to residual solar heat that was deposited in the ocean in the previous summer. From mid-November to January the ocean heat flux was ranged from 0 to 3 W m^{-2} . Even adjusting for

platelet ice, as described above, the mid-January value is -3.5 W m^{-2} . This negative value is a direct consequence of the deposited platelet ice that is incorporated into the growing ice. Platelet ice was also observed at the MOSAiC CO during this period (Katlein et al., 2020) and at some locations at the L3 remote floe (Lei et al., 2022). The ocean heat flux remained small in March and April and began to increase in May. There was a sharp increase in mid-June to 29 W m^{-2} . F_w reached a maximum of 75 W m^{-2} during the period June 26 to July 10. This increase was due to more solar heating of the upper ocean and the floe moving south toward the marginal ice zone and warmer water. The ocean heat fluxes observed at L2 are comparable to those reported for MOSAiC in Lei et al. (2022) and those reported for other times and regions (Krishfield and Perovich, 2005).

3.5. Snow effective thermal conductivity

Estimates of the bulk effective thermal conductivity of snow (k_s^*) were calculated using a technique presented in Sturm et al. (2002) assuming continuity of heat flux at the snow ice interface. Assuming heat flux continuity is simply stating that the heat flux out of the ice is equal to the heat flux into the snow.

$$k_i = \frac{dT_i}{dz_i} = k_s^* = \frac{dT_s}{dz_s} \quad (2)$$

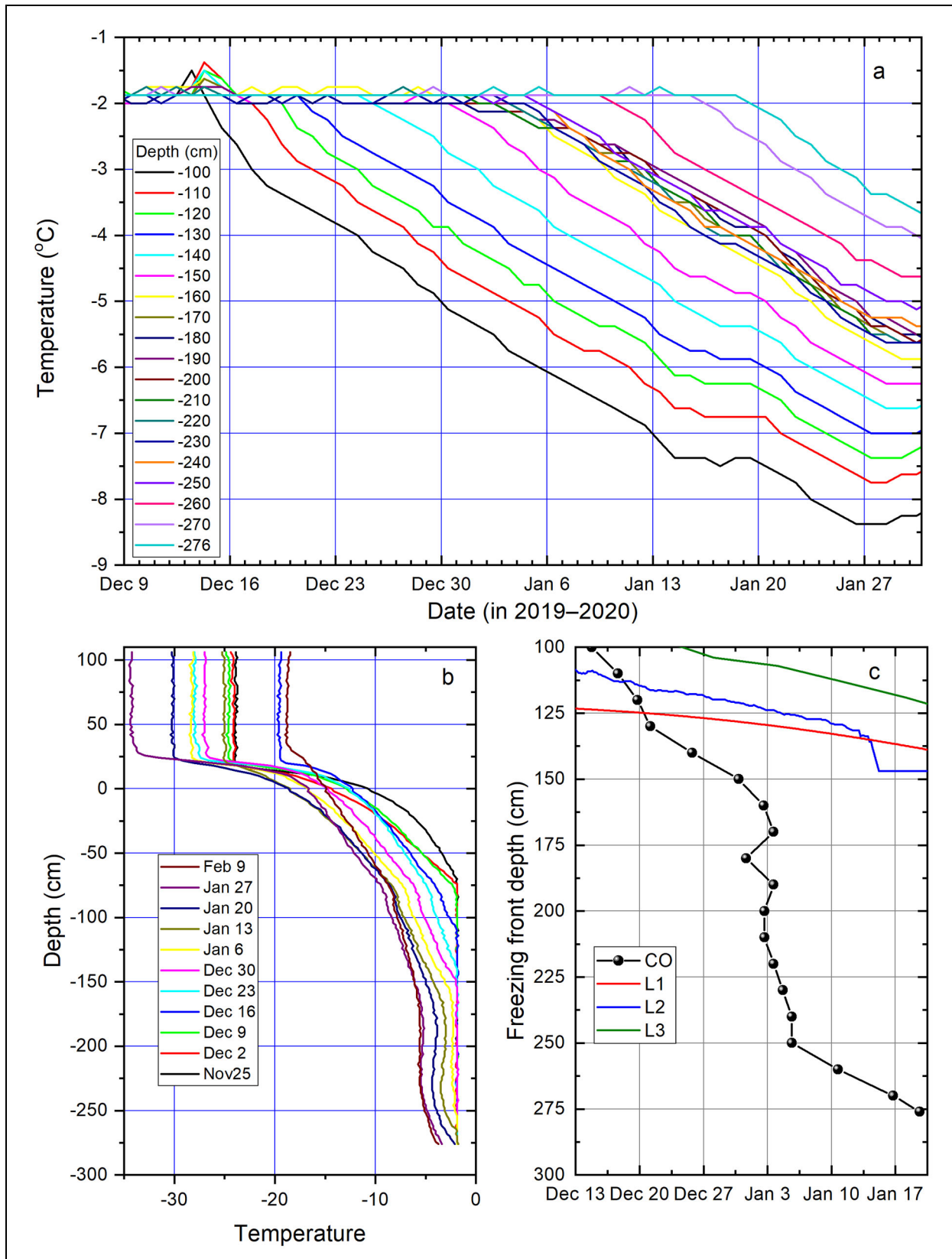


Figure 6. Temperature profiles from the four seasonal ice mass balance buoys. (a) Time series of ice temperatures at selected depths from the Central Observatory (CO) seasonal ice mass balance (SIMB) buoy. (b) Weekly vertical temperature profiles from the CO SIMB, where zero indicates the ice–snow interface. (c) Freezing front depth as a function of time for the four SIMBs (CO, L1, L2, and L3). The L1, L2, and L3 curves in panel (c) were determined from the under-ice sounder. The CO curve was derived from temperature profiles.

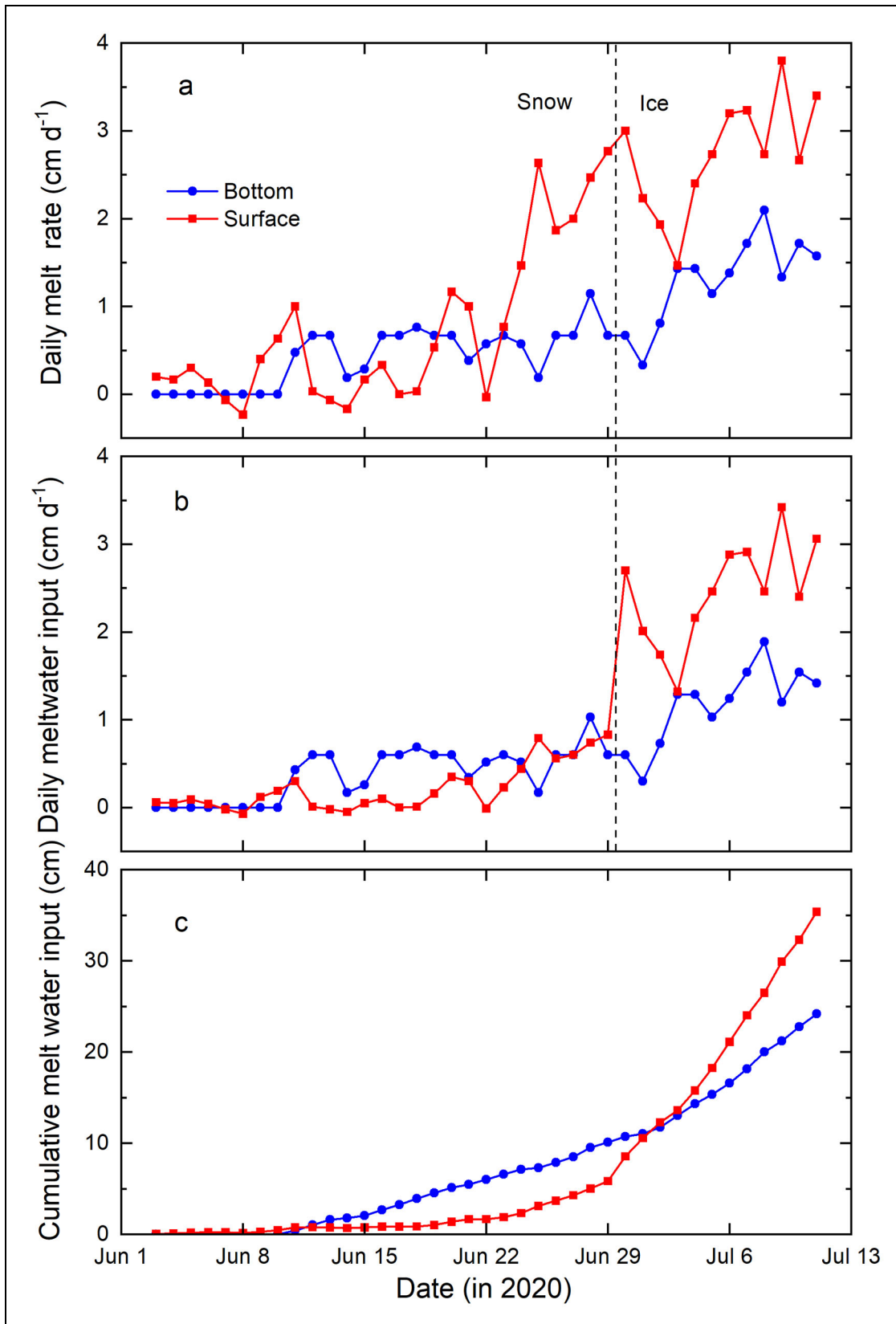


Figure 7. Time series of melt rate and meltwater input from sea ice balance buoy L2. Time series of (a) daily surface and bottom ice melt rate, (b) daily meltwater input, and (c) cumulative meltwater input. The dashed vertical line indicates when surface melting transitioned from snow to ice.

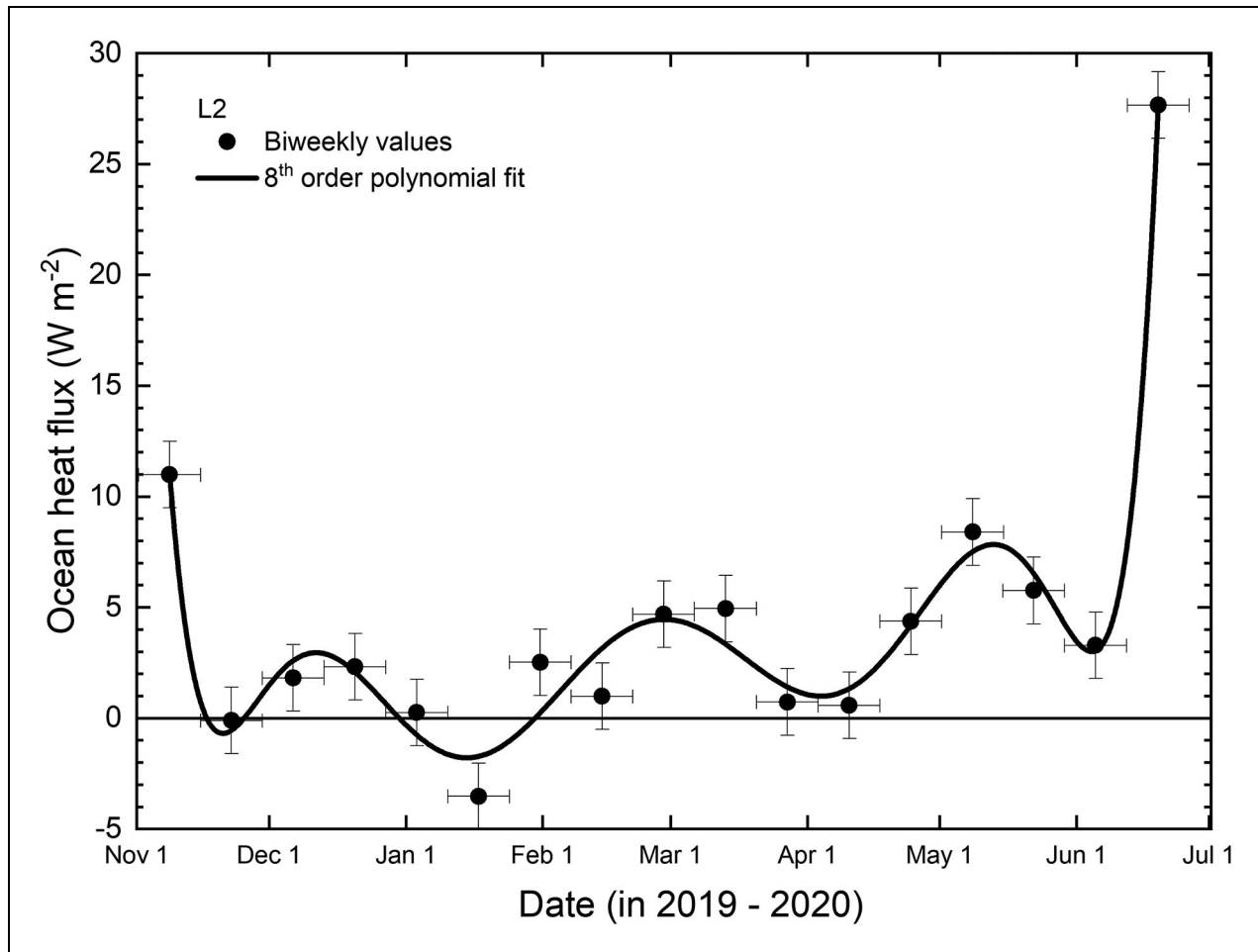


Figure 8. Values of ocean heat flux determined from sea ice balance buoy L2. The ocean heat was calculated over a 2-week interval. The points denote the middle of the interval and the horizontal bars show the 2-week time period. Vertical bars indicate an uncertainty of $\pm 1.5 \text{ W m}^{-2}$ in ocean heat flux.

Solving Equation 2 for k_s^* , gives

$$k_s^* = \frac{k_i \left[\frac{dT_i}{dz_i} \right]}{\left[\frac{dT_s}{dz_s} \right]}, \quad (3)$$

where the subscripts i and s denote snow and ice, T is the temperature, z is the depth, and k_i is the thermal conductivity of ice, again assumed to be $2 \text{ W m}^{-1} \text{ C}^{-1}$.

Temperature gradients in the snow and ice were determined from measured temperature profiles. A linear fit was applied to the six snow temperatures from 2 cm to 12 cm above the snow–ice interface to determine dT_s/dz_s . Similarly, temperatures from 2 cm to 12 cm below the snow–ice interface were used to determine dT_i/dz_i . We did not use the temperature sensor that was nominally at the interface due to small uncertainties in its exact position. This approach is predicated on three assumptions: (i) continuity of heat flux at the snow–ice interface, (ii) linearity of the temperature profiles in the snow and ice, and (iii) no snow–ice or superimposed ice formation.

Equation 3 was evaluated every 4 hours from December through mid-March for data from the L1 and L2 buoys. This period was selected to avoid complications from the freeze-in period (October–November) and from solar radiation (mid-March to end of experiment). The time series

for k_s^* and a 3-day running mean of k_s^* for L1 and L2 from December 1, 2019 to March 15, 2020 are plotted in **Figure 9**. Large and rapid changes in k_s^* are evident. There can be variations in k_s^* due to physical drivers such as wind pumping and the evolution of the snow cover (Sturm et al., 2002). However, most of the variability in **Figure 9** is likely due to the limitation of this approach. When air temperatures are changing rapidly, the temperature profiles in the snow and ice deviate from steady state and from linearity, causing errors in the estimate of k_s^* .

For the L1 buoy, the average k_s^* of all measurements was $0.42 \text{ W m}^{-1} \text{ }^\circ\text{C}^{-1}$, the median was $0.40 \text{ W m}^{-1} \text{ }^\circ\text{C}^{-1}$, and the standard deviation was $0.25 \text{ W m}^{-1} \text{ }^\circ\text{C}^{-1}$ (**Table 2**). For the L2 buoy, the average k_s^* was $0.47 \text{ W m}^{-1} \text{ }^\circ\text{C}^{-1}$, the median was $0.44 \text{ W m}^{-1} \text{ }^\circ\text{C}^{-1}$, and the standard deviation was $0.29 \text{ W m}^{-1} \text{ }^\circ\text{C}^{-1}$. The large standard deviations illustrate the limitations of using this approach when temperatures in the air, snow, and ice are changing rapidly and the temperature profiles are not linear.

Estimates of k_s^* can be improved by focusing on times when the temperature profiles were linear. For each k_s^* , coefficients of determination (R^2) were calculated for the linear fits of the snow and ice temperature profiles. The triangles in the **Figure 9** represent times when R^2 was greater than 0.99 for both the snow and ice temperature

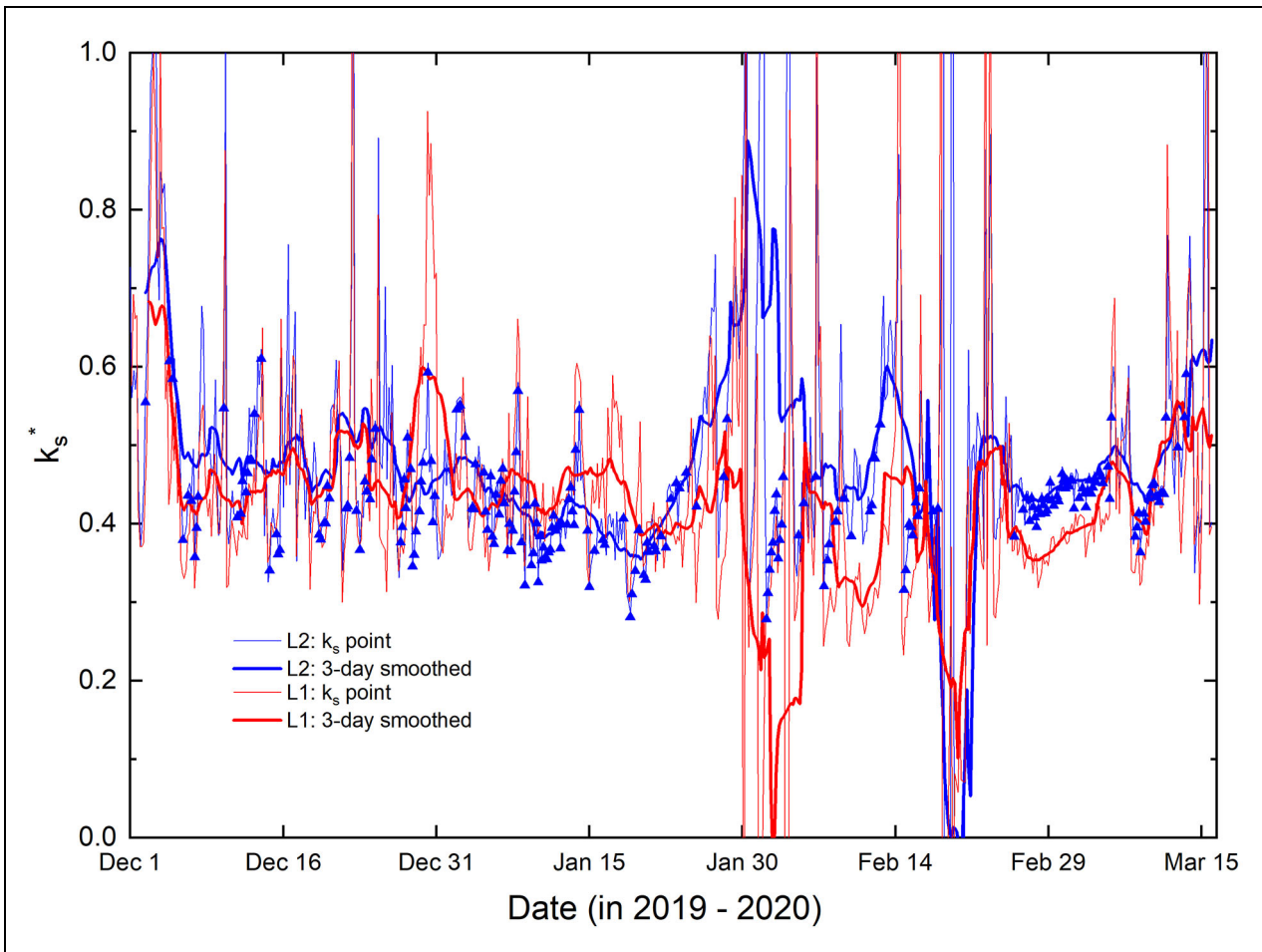


Figure 9. Time series of effective thermal conductivity of snow from two seasonal ice mass balance buoys. The time series of effective thermal conductivity, k_s^* , and a 3-day running mean of k_s^* obtained from seasonal ice mass balance buoys L1 and L2. The symbols denote times when $R^2 > 0.99$ for the linear fits in both the snow and in the ice.

Table 2. Statistical values for effective thermal conductivity of snow (k_s^*) from seasonal ice mass balance buoys L1 and L2, considering all cases and only cases when R^2 is greater than 0.99 for both snow and ice temperature profiles

Statistic	All Cases		Cases of $R^2 > 0.99$	
	L1	L2	L1	L2
Mean	0.42	0.47	0.41	0.42
Median	0.40	0.44	0.40	0.42
Standard deviation	0.25	0.29	0.075	0.058
N value	612	625	90	233

profiles. **Table 2** summarizes the results using all the data and using only data when R^2 was greater than 0.99 for both the snow and ice profiles.

Considering k_s^* only when $R^2 > 0.99$ for both the snow and the ice profiles reduced the number of cases from 612 to 90 for L1 and from 612 to 233 for L2. For L1, the mean k_s^* was $0.41 \text{ W m}^{-1} \text{ }^\circ\text{C}^{-1}$, the median 0.40, and the

standard deviation 0.07. For L2, the mean was $0.42 \text{ W m}^{-1} \text{ }^\circ\text{C}^{-1}$, the median 0.42, and the standard deviation 0.06. The standard deviation of k_s^* for both L1 and L2 is greatly reduced by applying the $R^2 > 0.99$ criteria. There was very little change in the mean and median for L1, while the L2 mean and median were reduced to 0.42.

There can be considerable variability in estimates of the effective thermal conductivity of snow. For example, Sturm et al. (2002), using the same approach as in this study, reported an average value for k_s^* of $0.33 \text{ W m}^{-1} \text{ }^\circ\text{C}^{-1}$ for measurements made during the SHEBA experiment in the Beaufort Sea in 1997 to 1998. The SHEBA value is smaller than k_s^* measured at either L1 or L2. Sturm et al. (2002) also reported a large range in k_s^* between sites, possibly due to the non-vertical transfer of heat. More research is needed to understand the full range of possible k_s^* values and to explain how snow physical properties, spatial variability in snow depth, and atmospheric forcing contribute to the observed variability in k_s^* .

4. Discussion

4.1. Mass balance comparison

Here we compare MOSAiC mass balance results to earlier observations made as part of the North Pole

Environmental Observatory (NPEO; Morison et al., 2002). Nine ice mass balance buoys were deployed in the Transpolar Drift near the North Pole during the period from 2000 to 2013 (Perovich et al., 2014). The results from the NPEO study are not a perfect comparison to MOSAiC as they were deployed near the North Pole in April, while MOSAiC was at 85°N in April. However, we can compare basic conditions between the NPEO buoys and the L2 SIMB.

The maximum snow depth at L2 was 0.24 m. NPEO maximum snow depths ranged from 0.04 m to 0.38 m, with a mean of 0.25 m. The maximum ice thickness at L2 was 1.90 m. NPEO ice thicknesses ranged from 1.77 m to 2.80 m, with an average of 2.27 m. The maximum snow depth at L2 is in the middle of the NPEO results. The L2 maximum thickness is within the range of the NPEO values, but in the lower third of the range.

Snow melt at L2 started on June 8, when L2 was at 83°N. The start of snow melt at the NPEO sites ranged from June 1 to June 15, with all buoy positions north of 87°N. The date of snow melt onset at L2 was in the middle of the NPEO range even though it was 450 km further south. Total amounts of melting cannot be compared because the MOSAiC floe was abandoned at the end of July. Past results indicate that surface melting usually ends in mid-August and bottom melt can last until the end of September. The total surface melt at L2 was 0.39 m, falling within the NPEO range of 0.13 m to 0.56 m. With additional weeks of surface melt, L2 would likely be at the high end of the NPEO range. The L2 bottom melt of 0.30 m is on the high end of the NPEO range of 0.15 m to 0.57 m. This position in the range is not surprising as at the end of July, L2 was more than 600 km further south than the NPEO buoys and in the marginal ice zone.

The details of the L2 melt amounts are moot, as the floe exited Fram Strait and all the ice melted after the floe was abandoned. The floe would likely have survived summer melt had it been further from the ice edge. The largest difference between L2 and the NPEO results is the floe velocity. The average daily drift from May through July was 11.3 km for L2 compared to an average of 4.1 km for the NPEO buoys. The rapid drift of the MOSAiC floe was responsible for the loss of the floe (Krumpfen et al., 2021).

4.2. Onset of ice growth

Analyzing results from MOSAiC, Lei et al. (2022) defined four phases of ice mass balance: freezing onset, rapid ice growth, slowly growing, and melting. The timing of these phases strongly influences the thermodynamic evolution of the sea ice cover. Satellite remote sensing has been used to map the spatial and temporal variability of the onset dates of surface melt onset and freezeup (Markus et al., 2009). While satellites observe conditions on the surface, they do not see what is happening on the bottom of the ice.

Planck et al. (2020) used results from autonomous ice mass balance buoys to determine dates for beginning of snow melt, surface ice melt, and bottom ice melt and for ending surface melt and bottom melt for eight sites in the Beaufort Sea for 8 different years. They found variations

ranging from 13 days (beginning of bottom melt) to 47 days (beginning of surface ice melt). This variability is not surprising given that the results were from different years at different locations within the Beaufort Sea.

MOSAiC provided an opportunity to examine the local variability in onset dates for 1 year. The atmospheric and oceanic forcings were generally the same at all the MOSAiC locations. Here we examine the first phase of the Lei et al. (2022) sequence, the onset of basal growth. **Figure 10** shows the onset date of basal growth versus the initial ice thickness for three second-year MOSAiC sites (CO, L1, L2) and four multiyear sites from SHEBA (Perovich and Elder, 2001). There was an additional SHEBA site that was an 8-m-thick ridge where basal freezing never started. As expected, both MOSAiC and SHEBA have a general trend of thicker ice leading to later basal freezing.

There are two data points (see arrows in **Figure 10**) of particular interest. One from SHEBA was 0.9-m-thick ice where basal growth did not start until December 20, 1997, several weeks later than ice that was twice as thick. This site was ponded ice. Basal growth could not begin until the pond had frozen. Slowing basal growth further was deep snow that drifted onto the freezing pond (Perovich et al., 2003). The other point was the MOSAiC L1 site. This delay in the onset of basal growth was due to the large voids in the ice filled with brine. Propagating the cold front through the ice was not just cooling the ice, but freezing the large amount of brine. Large voids of brine can be found in sea ice at the end of summer (Barber et al., 2009). This analysis demonstrates that the timing of basal

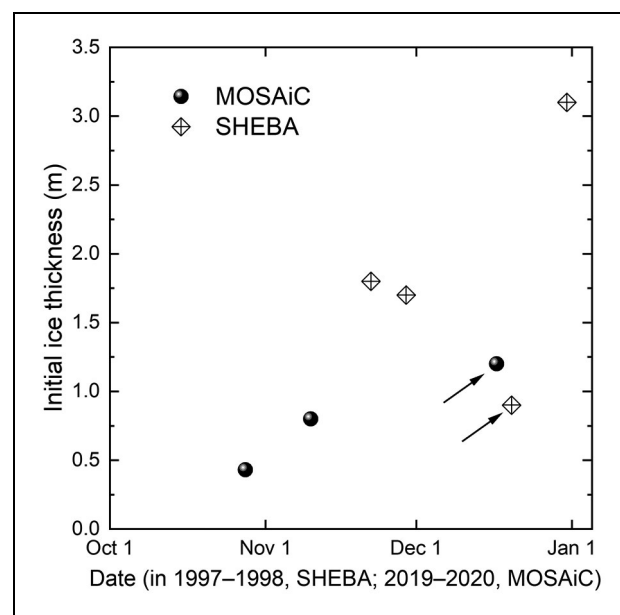


Figure 10. Onset of basal ice growth versus ice thickness. The onset date of basal ice growth versus the end-of-summer initial ice thickness for three MOSAiC second-year ice sites and four SHEBA multiyear ice sites. The arrows denote two special cases of delayed basal growth. For the SHEBA site, a melt pond had to freeze first; for the L1 MOSAiC site, large void spaces in the ice were filled with brine.

growth onset depends not only on ice thickness but also on ponding and the internal state of the ice.

4.3. Conductive heat flux

The variability of snow depth and ice thickness strongly influences heat conduction to the surface. A complex field of spatially varying snow depths and ice thicknesses is often treated using an average snow depth and an average ice thickness. This approach is inaccurate because the conductive flux varies as dT/dz . Difficulty in determining the heat conduction through an area is compounded by the uncertainty in the value of k_s^* .

Here we calculate the conductive heat flux to the surface for a sample case using observations of snow depth and ice thickness from a transect made on March 5, 2020, during MOSAiC (Itkin et al., 2023). The approach is based on six assumptions: (1) the heat flow is one dimensional in the vertical; (2) the temperature at the bottom of the ice is equal to the water temperature (T_w); (3) the temperature at the surface of the snow is equal to the air temperature (T_a); (4) temperature profiles in the snow and ice are linear; (5) the thermal conductivities are constant with depth; and (6) the conductive heat flux is continuous at the snow–ice interface.

We used air and water temperatures from the L2 SIMB. The spatial distribution of snow depth (h_s) and ice thickness (H_i) were obtained from survey transects (Nicolaus et al., 2022; Itkin et al., 2023). The linearity of the temperature profiles was assessed from SIMB results. Taking a one-time snapshot and assuming 1-D heat flow are major simplifications, and they both will accentuate the impact of spatial variability. This analysis thus represents a maximum impact of spatial variability.

Given the assumptions above, the conductive flux through the snow is

$$F_s = k_s^* \frac{dT}{dz} = k_s^* \frac{(T_a - T_{si})}{h_s} \quad (4)$$

We do not know the value of T_{si} along the transect line. Assumption 5 is $F_s = F_i$, giving

$$k_s^* \frac{(T_a - T_{si})}{h_s} = k_i \frac{(T_{si} - T_w)}{H_i} \quad (5)$$

Solving Equation (5) for T_{si} and substituting into Equation (4) gives the conductive flux through the snow (F_c)

$$F_c = \gamma(T_w - T_a) \quad (6)$$

where, following the formulation of Maykut (1978),

$$\gamma = \frac{k_i k_s^*}{(k_s^* H_i + k_i h_s)}. \quad (7)$$

Equations (6) and (7) were evaluated to determine the conductive heat flux through the snow at each point along the transect. These individual values were averaged to calculate the average for the entire transect ($\overline{F_c}$). For comparison, an average conductive heat flux was also calculated using the average snow depth and ice thickness from the transect (F_c^{ave}).

F_c was calculated using transect results from March 5, 2020. This date was selected because: (i) darkness still

prevailed in early March; (ii) air temperatures were cold; and (iii) air temperatures were stable. The following values were used to compute F_c : $T_a = -40^\circ\text{C}$, $T_w = -1.8^\circ\text{C}$, $k_s^* = 0.4 \text{ W m}^{-1} \text{ }^\circ\text{C}^{-1}$, and $k_i = 2.0 \text{ W m}^{-1} \text{ }^\circ\text{C}^{-1}$.

Pairs of snow depth and ice thickness for South Loop (Itkin et al., 2023) are plotted in **Figure 11a**. There is a wide range of ice thicknesses and snow depths. Much of the ice was about 1.5 m thick, with a few pressure ridges. The mean and median ice thicknesses were 1.69 m and 1.45 m. The mean and median snow depths were 0.25 m and 0.21 m. Conductive fluxes ranged from 9.9 W m^{-2} to 45.4 W m^{-2} , with an average of the individual fluxes ($\overline{F_c}$) (black line in **Figure 11a**) equal to 28.9 W m^{-2} . The conductive flux using the average snow depth and ice thickness (F_c^{ave}) was 26.1 W m^{-2} , 2.8 W m^{-2} (9.7%) smaller than the average of all the heat conduction values ($\overline{F_c}$). Calculating the average heat flux by averaging the flux at all the points ($\overline{F_c}$) always results in a larger value than calculating the average flux by using the average snow depth and ice thickness (F_c^{ave}).

The results in **Figure 11** use $k_s^* = 0.4$ and $k_i = 2.0 \text{ W m}^{-1} \text{ }^\circ\text{C}^{-1}$. **Figure 12** explores the impact of changing k_s^* on the values of $\overline{F_c}$ and F_c^{ave} . In all cases as k_s^* increases, the conductive heat flux increases. However, the increase in conductive heat flux is tempered. For example, doubling k_s^* from 0.25 to 0.50 increases $\overline{F_c}$ by only 32%. Using the Sturm et al. (2002) k_s^* of $0.33 \text{ W m}^{-1} \text{ }^\circ\text{C}^{-1}$ results in an $\overline{F_c} = 26.7 \text{ W m}^{-2}$, only 2.2 W m^{-2} (8%) less than the value computed using $k_s^* = 0.4$. For the March 5, 2020, case, the 8% reduction in calculated heat conduction using $k_s^* = 0.33$ is comparable to the reduction of 10% using mean snow depths and ice thicknesses.

5. Conclusions

As part of a larger ice mass balance observation network, four autonomous mass balance buoys were deployed during MOSAiC, three at remote sites and one at the CO. Three buoys were deployed in second-year ice and one in first-year ice. Air temperatures were similar to within a few degrees at all four sites. In contrast, snow–ice interface temperatures varied by up to 10°C due to one site having a much deeper snow cover. Initial ice thicknesses at the four sites in October ranged from 0.3 m to 1.4 m. The onset of basal ice growth for the second-year ice ranged from October 28 to December 17. The timing of basal growth onset depended not only on ice thickness but also on the internal state of the ice. By February 1, 2020, the range of ice thicknesses had decreased to 1.31–1.46 m. The thin first-year ice had almost caught up to the thicker second-year ice. By July 12, surface melt produced more meltwater than bottom melt (0.35 m versus 0.25 m).

Estimates of ocean heat flux ranged from 0 to 3 W m^{-2} for most of the winter. The exception was in January when an ephemeral period of platelet ice formation resulted in an ocean heat flux of -5 W m^{-2} . This negative value was due to the supercooling of the seawater under the ice, and the accumulation of platelet ice at the ice bottom augmenting ice growth. In June, the combination of increased solar heating of the upper ocean and proximity of the floe to the warmer waters of the marginal ice zone resulted in

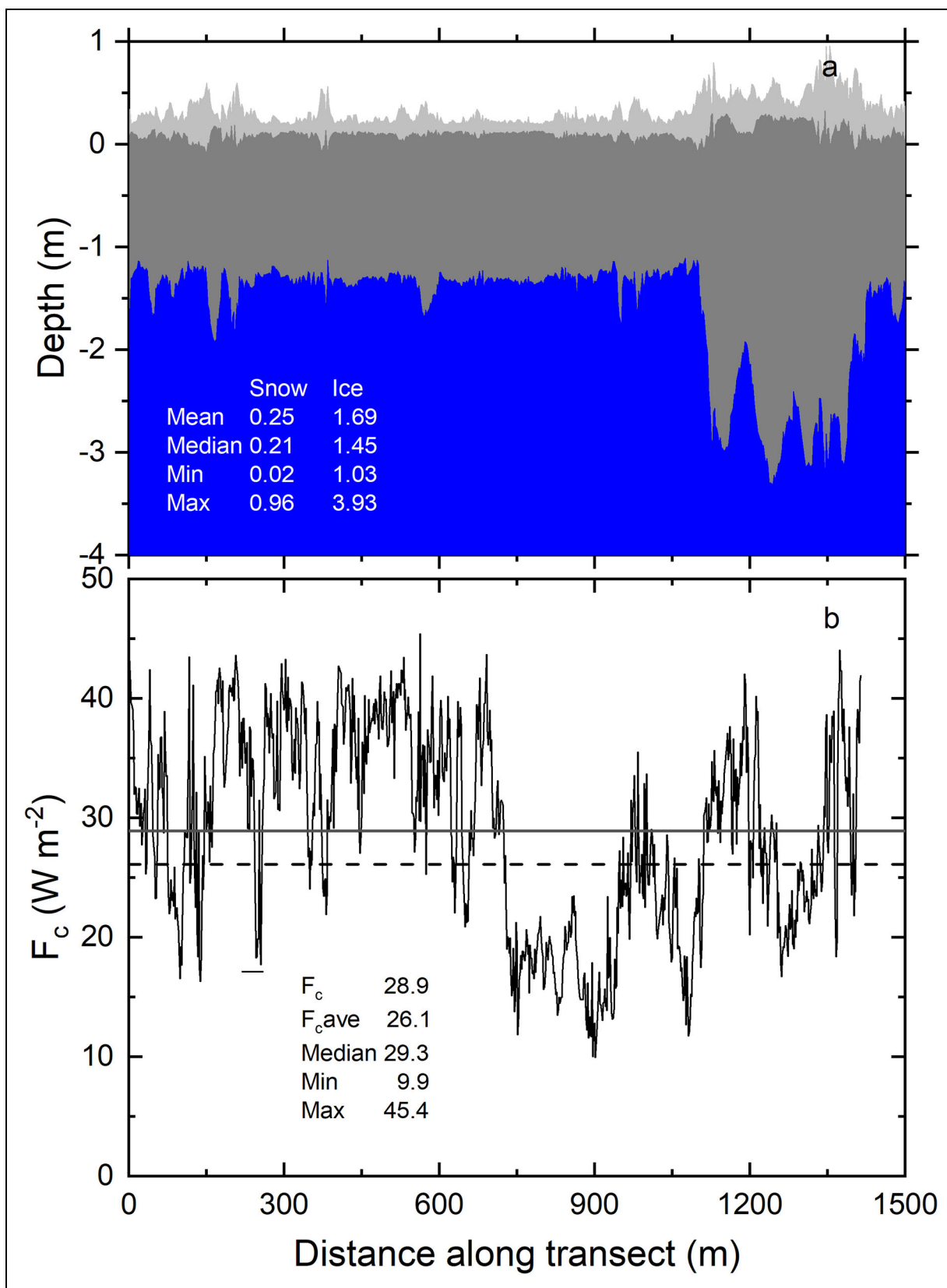


Figure 11. Heat conduction through the snow on a transect in March 2023. (a) Snow depth and ice thickness along the South Loop transect (Itkin et al., 2023) measured on March 5, 2023, and (b) the point-by-point heat conduction through the snow. Measurements were made at 944 points along a 1500-m-long line. The solid black line is the average of all the heat fluxes (F_c), and the dashed line is the heat conduction using the average snow depth and ice thickness (F_c^{ave}).

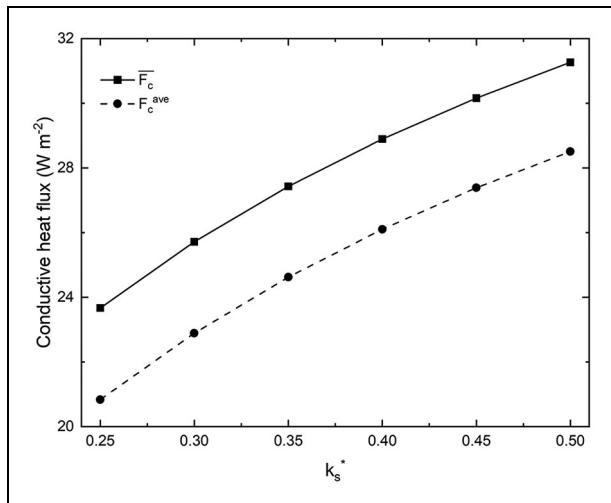


Figure 12. Conductive heat flux as a function of the effective thermal conductivity of snow (k_s^*). Average conductive heat flux along the South Loop transect line (Itkin et al., 2023) on March 5, 2020, as a function of effective thermal conductivity of snow (k_s^*). The solid black line is the average of all the heat fluxes ($\overline{F_c}$), and the dashed line is the heat conduction using the average snow depth and ice thickness (F_c^{ave}).

a rapid increase in ocean heat flux reaching a maximum of 75 W m^{-2} . These values were comparable to other MOSAiC observations (Lei et al., 2022).

Estimates of average effective snow thermal conductivity derived from all snow and ice temperature data from December 1, 2019, to March 15, 2020, were $0.42 \text{ W m}^{-1} \text{ }^\circ\text{C}^{-1}$ at L1 and $0.47 \text{ W m}^{-1} \text{ }^\circ\text{C}^{-1}$ at L2. By focusing on periods with linear temperature gradients in the snow and ice, values were refined to $0.41 \text{ W m}^{-1} \text{ }^\circ\text{C}^{-1}$ at L1 and $0.42 \text{ W m}^{-1} \text{ }^\circ\text{C}^{-1}$ at L2. These values are larger than the $0.33 \text{ W m}^{-1} \text{ }^\circ\text{C}^{-1}$ reported in Sturm et al. (2002) determined using the same technique. The drivers of the differences in k_s^* within MOSAiC and between MOSAiC and SHEBA still need to be determined. Using average values of snow depth and ice thickness to calculate the areally averaged conductive flux results in values less than those resulting from calculating fluxes at individual points and then averaging.

In many ways ice conditions at the L2 site were similar to those observed during the 9 years of the North Pole Environmental Observatory. The maximum snow depth and ice thickness were within the NPEO range, as was the onset date of surface melt. There were two major differences: the presence of platelet ice in the winter (Katlein et al., 2020) and the rapid motion of MOSAiC (Krumpfen et al., 2021). The platelet ice formation was an interesting, ephemeral event that, combined with observations at the CO (Katlein et al., 2020), demonstrated that the platelet ice was widespread. The rapid ice motion was responsible for the demise of the MOSAiC floe. At the end of July, the ice thickness at L2 was 1.3 m, which normally would have been sufficient to survive the summer. However, because of its rapid transit, it was exiting the marginal ice zone of Fram Strait into warm waters. More research is needed to

determine if the drift of MOSAiC in 2019–2020 was an anomaly or a harbinger.

The next step is to integrate these results with other MOSAiC observations. Mass balance results could be combined with the extensive observations of the surface heat budget to investigate the relative magnitude of the conductive flux and determine if the heat budget can be closed. Synthesis of the ocean heat flux estimates and physical oceanographic measurements will facilitate studies of ice–ocean interactions. Finally, the larger scale implications of these findings, such as delayed basal ice growth and the variability in k_s^* , should be explored in single column models.

Data accessibility statement

All of the buoy data used in this article have been submitted and archived in the Arctic Data Center. The DOI for this archived dataset is <https://doi.org/10.18739/A20Z70Z01>.

Acknowledgments and funding

Data used in this manuscript were produced as part of the international Multidisciplinary drifting Observatory for the Study of the Arctic Climate (MOSAiC) with the tag MOSAiC20192020 and the Project_ID: AWI_PS122_00. The authors thank all people involved in the expedition of the Research Vessel *Polarstern* (Knust, 2017) during MOSAiC in 2019–2020 as listed in Nixdorf et al. (2021). DP, IR, DC-S, and CP were supported by the NSF–OPP–1724540, NSF–OPP–1724424, and NSF –OPP–2034919, RM by the MOSAiC School, RL by the National Natural Science Foundation of China (41976219), and AS by the DOE Atmospheric System Research Program (DE-SC0021341) and NOAA cooperative agreement NA22OAR4320151. The authors also thank Tim Stanton, Thomas Krumpfen, Thea Schneider, Lisa Craw, Igor Vasilevich, Michel Tsamados, and David Wagner for their help installing the buoys.

Competing interests

The authors declare that they have no conflict of interest.

Author contributions

All authors contributed to the writing, editing, and approval of the article and to the analysis of the data. DP formulated the initial design of the manuscript. RM, IR, and DC-S contributed to the installation and maintenance of the buoys.

References

- Barber, D, Galley, R, Asplin, M, DeAbreu, R, Warner, K-A, Pucko, M, Gupta, M, Prinsenbery, S, Julien, S. 2009. Perennial pack ice in the southern Beaufort Sea was not as it appeared in the summer of 2009. *Geophysical Research Letters* **36**(24): L24501. DOI: <http://dx.doi.org/10.1029/2009GL041434>.
- Belter, HJ, Krumpfen, T, von Albedyll, L, Alekseeva, TA, Birnbaum, G, Frolov, SV, Hendricks, S, Herber, A, Polyakov, I, Raphael, I, Ricker, R, Serovetnikov, SS, Webster, M, Haas, C. 2021. Interannual variability in Transpolar Drift summer sea ice thickness and potential impact of Atlantification. *The*

- Cryosphere* **15**(6): 2575–2591. DOI: <http://dx.doi.org/10.5194/tc-15-2575-2021>.
- Itkin, P, Hendricks, S, Webster, M, von Albedyll, L, Arndt, S, Divine, D, Jaggi, M, Oggier, M, Raphael, I, Ricker, R, Rohde, J, Schneebeli, M, Liston, G.** 2023. Sea ice and snow characteristics from year-long transects at the MOSAiC Central Observatory. *Elementa: Science of the Anthropocene* **11**(1): 00048. DOI: <http://dx.doi.org/10.1525/elementa.2022.00048>.
- Katlein, C, Mohrholz, V, Sheikin, I, Itkin, P, Divine, DV, Stroeve, J, Jutila, A, Krampe, D, Shimanchuk, E, Raphael, I, Rabe, B, Kuznetsov, I, Mallet, M, Liu, H, Hoppmann, M, Fang, YC, Dumitrascu, A, Arndt, S, Anhaus, P, Nicolaus, M, Matero, I, Oggier, M, Eicken, H, Haas, C.** 2020. Platelet ice under Arctic pack ice in winter. *Geophysical Research Letters* **47**(16): e2020GL088898.
- Knust, R.** 2017. Polar research and supply vessel POLARSTERN operated by the Alfred-Wegener Institute. *Journal of Large-Scale Research Facilities JLSRP* **3**: 119.
- Krishfield, RA, Perovich, DK.** 2005. Spatial and temporal variability of oceanic heat flux to the Arctic ice pack. *Journal of Geophysical Research: Oceans* **110**(C7): C07021. DOI: <http://dx.doi.org/10.1029/2004JC002293>.
- Kruppen, T, Birrien, F, Kauker, F, Rackow, T, von Albedyll, L, Angelopoulos, M, Belter, HJ, Bessonov, V, Damm, E, Dethloff, K, Haapala, J, Haas, C, Harris, C, Hendricks, S, Hoelemann, J, Hoppmann, M, Kaleschke, L, Karcher, M, Kolabutin, N, Lei, R, Lenz, J, Morgenstern, A, Nicolaus, M, Nixdorf, U, Petrovsky, T, Rabe, B, Rabenstein, L, Rex, M, Ricker, R, Rohde, J, Shimanchuk, E, Singha, S, Smolyanitsky, V, Sokolov, V, Stanton, T, Timofeeva, A, Tsamados, M, Watkins, D.** 2020. The MOSAiC ice floe: Sediment-laden survivor from the Siberian shelf. *The Cryosphere* **14**(7): 2173–2187. DOI: <http://dx.doi.org/10.5194/tc-14-2173-2020>.
- Kruppen, T, von Albedyll, L, Goessling, HF, Hendricks, S, Juhls, B, Spreen, G, Willmes, S, Belter, HJ, Dethloff, K, Haas, C, Kaleschke, L, Katlein, C, Tian-Kunze, X, Ricker, R, Rostosky, P, Rückert, J, Singha, S, Sokolova, J.** 2021. MOSAiC drift expedition from October 2019 to July 2020: Sea ice conditions from space and comparison with previous years. *The Cryosphere* **15**(8): 3897–3920. DOI: <http://dx.doi.org/10.5194/tc-15-3897-2021>.
- Kwok, R.** 2018. Arctic sea ice thickness, volume, and multiyear ice coverage: Losses and coupled variability (1958–2018). *Environmental Research Letters* **13**(10): 105005. DOI: <http://dx.doi.org/10.1088/1748-9326/aae3ec>.
- Kwok, R, Markus, T, Kurtz, NT, Petty, AA, Neumann, TA, Farrell, SL, Cunningham, GF, Hancock, DW, Ivanoff, A, Wimert, JT.** 2019. Surface height and sea ice freeboard of the Arctic Ocean from ICESat-2: Characteristics and early results. *Journal of Geophysical Research* **124**(10): 6942–6959. DOI: <http://dx.doi.org/10.1029/2019JC015486>.
- Lei, R, Cheng, B, Heil, P, Vihma, T, Wang, J, Ji, Q, Zhang, Z.** 2018. Seasonal and interannual variations of sea ice mass balance from the Central Arctic to the Greenland Sea. *Journal of Geophysical Research: Oceans* **123**(4): 2422–2439. DOI: <http://dx.doi.org/10.1002/2017JC013548>.
- Lei, R, Cheng, B, Hoppmann, M, Zhang, F, Zuo, G, Hutchings, JK, Lin, L, Lan, M, Wang, H, Regnery, J, Krumpfen, T, Rabe, B, Perovich, D, Nicolaus, M.** 2022. Seasonality and timing of sea ice mass and heat fluxes in the Arctic transpolar drift during 2019–2020. *Elementa: Science of the Anthropocene* **10**(1): 000089. DOI: <http://dx.doi.org/10.1525/elementa.2021.000089>.
- Markus, T, Stroeve, JC, Miller, J.** 2009. Recent changes in Arctic sea ice melt onset, freezeup, and melt season length. *Journal of Geophysical Research* **114**(C12): C12024. DOI: <http://dx.doi.org/10.1029/2009JC005436>.
- Maslanik, J, Stroeve, J, Fowler, C, Emery, W.** 2011. Distribution and trends in Arctic sea ice age through spring 2011. *Geophysical Research Letters* **38**(13). DOI: <http://dx.doi.org/10.1029/2011GL047735>.
- Maykut, G.** 1978. Energy exchange over young sea ice in the central Arctic. *Journal of Geophysical Research* **83**(C7): 3646–3658. DOI: <http://dx.doi.org/10.1029/JC083iC07p03646>.
- Maykut, G, McPhee M.** 1995. Solar heating of the Arctic mixed layer. *Journal of Geophysical Research* **100**(C12): 24691–24703.
- McPhee, M.** 1992. Turbulent heat flux in the upper ocean under sea ice. *Journal of Geophysical Research* **97**(C4): 5365–5379.
- McPhee, M, Untersteiner, N.** 1982. Using sea ice to measure vertical heat flux in the ocean. *Journal of Geophysical Research* **87**(C3): 2071–2074.
- Meier, WN, Hovelsrud, GK, Van Oort, BE, Key, JR, Kovacs, KM, Michel, C, Haas, C, Granskog, MA, Gerland, S, Perovich, DK, Makshtas, A.** 2014. Arctic sea ice in transformation: A review of recent observed changes and impacts on biology and human activity. *Reviews of Geophysics* **52**(3): 185–217. DOI: <http://dx.doi.org/10.1002/2013RG000431>.
- Meier, WN, Perovich, D, Farrell, S, Haas, C, Hendricks, S, Petty, AA, Webster, M, Divine, D, Gerland, S, Kaleschke, L, Ricker, R, Steer, A, Tian-Kunze, X, Tschudi, M, Wood, K.** 2021. Sea Ice. Arctic Report Card Sea Ice, NOAA Technical Report OAR ARC, 21–05. DOI: <http://dx.doi.org/10.25923/y2wd-fn85>.
- Morison, JA, Aagaard, K, Falkner, KK, Hatakeyama, K, Moritz, R, Overland, JE, Perovich, DK, Shimada, K, Steele, M, Takizawa, T, Woodgate, R.** 2002. North Pole Environmental Observatory delivers early results. *EOS, Transactions of the American Geophysical Union* **83**(33): 357, 360–361.
- Nicolaus, M, Perovich, DK, Spreen, G, Granskog, MA, von Albedyll, L, Anhaus, P, Angelopoulos, M, Arndt, A, Belter, HJ, Bessonov, V, Birnbaum, G, Brauchle, JB, Calmer, R, Cardellach, E, Cheng, B,**

- Clemens-Sewall, D, Dadic, R, Damm, E, de Boer, G, Demir, O, Divine, D, Fong, A, Fons, S, Fuchs, N, Gabarró, C, Gerland, S, Gradinger, R, Goessling, HF, Haapala, J, Haas, C, Hamilton, J, Hannula, HR, Hendricks, S, Herber, A, Heuzé, C, Hoppmann, M, Høyland, KV, Huntemann, M, Hutchings, JK, Hwang, B, Itkin, P, Jaggi, M, Jutila, A, Kaleschke, L, Katlein, C, Kolabutin, N, Krampe, D, Kristensen, SS, Krumpfen, T, Kurtz, N, Lampert, A, Lange, BA, Lei, R, Light, B, Linhardt, F, Liston, G, Loose, B, Macfarlane, AR, Mahmud, M, Matero, IO, Maus, S, Morgenstern, A, Naderpour, R, Nandan, V, Niubom, A, Oggier, M, Oppelt, N, Pätzold, F, Petrovsky, T, Pirazzini, R, Polashenski, C, Rabe, B, Raphael, IA, Regnery, J, Rex, M, Ricker, R, Riemann-Campe, K, Rinke, A, Rohde, J, Salganik, E, Scharien, RK, Schiller, M, Schneebeli, M, Semmling, M, Sheikin, I, Shimanchuk, E, Shupe, MD, Smith, MM, Smolyanitsky, V, Sokolov, V, Sokolova, J, Stanton, TP, Stroeve, J, Tavri, A, Thielke, L, Timofeeva, A, Tonboe, RT, Tsamados, M, Wagner, DN, Watkins, D, Webster, M, Wendisch, M. 2022. Overview of the MOSAiC expedition: Snow and sea ice. *Elementa: Science of the Anthropocene* **10**(1): 000046. DOI: <http://dx.doi.org/10.1525/elementa.2021.000046>.
- Nixdorf, U, Dethloff, K, Rex, M, Shupe, M, Sommerfeld, A, Perovich, DK, Nicolaus, M, Heuzé, C, Rabe, B, Loose, B, Damm, E, Gradinger, R, Fong, A, Maslowski, W, Rinke, A, Kwok, R, Spreen, G, Wendisch, M, Herber, A, Hirsekorn, M, Mohaupt, V, Frickenhaus, S, Immerz, A, Weiss-Tuider, K, König, B, Mengedoht, D, Regnery, J, Gerchow, P, Ransby, D, Krumpfen, T, Morgenstern, A, Haas, C. 2021. MOSAiC extended acknowledgement. Zenodo. DOI: <https://doi.org/10.5281/zenodo.5179738>.
- Perovich, D, Raphael, I, Moore, R, Clemens-Sewall, D, Polashenski, C, Planck, C. 2022. Measurements of ice mass balance and temperature from autonomous seasonal ice mass balance buoys in the Arctic Ocean, 2019–2020. Arctic Data Center. DOI: <http://dx.doi.org/10.18739/A20Z70Z01>.
- Perovich, DK, Elder, B. 2001. Temporal evolution and spatial variability of the temperature of Arctic sea ice. *Annals of Glaciology* **33**: 207–212.
- Perovich, DK, Grenfell, TC, Richter-Menge, JA, Light, B, Tucker, WB III. 2003. Thin and thinner: Sea ice mass balance measurements during SHEBA. *Journal of Geophysical Research* **108**(C3). DOI: <https://doi.org/10.1029/2001JC001079>.
- Perovich, DK, Richter-Menge, JA. 2015. Regional variability in sea ice melt in a changing Arctic. *Proceedings of the Royal Society* **373**(2045): 20140165. DOI: <http://dx.doi.org/10.1098/rsta.2014.0165>.
- Perovich, DK, Richter-Menge, JA, Polashenski, C, Elder, B, Arbetter, T, Brennick, O. 2014. Sea ice mass balance observations from the North Pole Environmental Observatory. *Geophysical Research Letters* **41**(6): 2019–2025. DOI: <http://dx.doi.org/10.1002/2014GL059356>.
- Planck, C, Perovich, D, Light, B. 2020. A synthesis of observations and models to assess the time series of sea ice mass balance in the Beaufort Sea. *Journal of Geophysical Research: Oceans* **125**(11): e2019JC015833. DOI: <http://dx.doi.org/10.1029/2019JC015833>.
- Planck, C, Whitlock, J, Polashenski, C, Perovich, D. 2019. The evolution of the seasonal ice mass balance buoy. *Cold Regions Science and Technology* **165**: 102792. DOI: <http://dx.doi.org/10.1016/j.coldregions.2019.102792>.
- Polashenski, C, Perovich, DK, Richter-Menge, JA, Elder, B. 2011. Autonomous observations of sea ice mass balance in seasonal ice. *Annals of Glaciology* **52**: 18–26.
- Rabe, B, Cox, CJ, Fang, Y-C, Goessling, H, Granskog, MA, Hoppmann, M, Hutchings, JK, Krumpfen, T, Kuznetsov, I, Lei, R, Li, T, Maslowski, W, Nicolaus, M, Perovich, D, Persson, O, Regnery, J, Rigor, I, Shupe, MD, Sokolov, V, Spreen, G, Stanton, T, Watkins, DM, Blockley, E, Buenger, HJ, Cole, S, Fong, A, Haapala, J, Heuzé, C, Hoppe, CJM, Janout, M, Jutila, A, Katlein, C, Krishfield, R, Lin, L, Ludwig, V, Morgenstern, A, O'Brien, J, Zurita, AQ, Rackow, T, Riemann-Campe, K, Rohde, J, Shaw, W, Smolyanitsky, V, Solomon, A, Sperling, A, Tao, R, Toole, J, Tsamados, M, Zhu, J, Zuo, G. n.d. The MOSAiC Distributed Network: Observing the coupled Arctic system with multidisciplinary, coordinated, platforms. *Elementa: Science of the Anthropocene*, submitted, under review.
- Smith, MM, von Albedyll, L, Raphael, IA, Lange, BA, Matero, I, Salganik, E, Webster, MA, Granskog, MA, Fong, A, Lei, R, Light, B. 2022. Quantifying false bottoms and under-ice meltwater layers beneath Arctic summer sea ice with fine-scale observations. *Elementa: Science of the Anthropocene* **10**(1): 000116. DOI: <http://dx.doi.org/10.1525/elementa.2021.000116>.
- Stroeve, JC, Kattsov, V, Barrett, A, Serreze, M, Pavlova, T, Holland, M, Meier, WN. 2012. Trends in Arctic sea ice extent from CMIP5, CMIP3 and observations. *Geophysical Research Letters* **39**(16): 1–7. DOI: <http://dx.doi.org/10.1029/2012GL052676>.
- Stroeve, JC, Markus, T, Boisvert, L, Miller, J, Barrett, A. 2014. Changes in Arctic melt season and implications for sea ice loss. *Geophysical Research Letters* **41**(4): 1216–1225. DOI: <http://dx.doi.org/10.1002/2013GL058951>.
- Sturm, M, Holmgren, J, Perovich, D. 2002. Thermal conductivity and heat transfer through the snow on the ice of the Beaufort Sea. *Journal of Geophysical Research* **107**(C10): SHE 19-1–19-17. DOI: <http://dx.doi.org/10.1029/2000JC000409>.
- Tschudi, MA, Stroeve, JC, Stewart, JS. 2016. Relating the age of Arctic sea ice to its thickness, as measured during NASA's ICESat and IceBridge Campaigns. *Remote Sensing* **8**(6): 457. DOI: <http://dx.doi.org/10.3390/rs8060457>.
- Wettlaufer, JS. 1991. Heat flux at the ice–ocean interface. *Journal of Geophysical Research* **96**(C4): 7215–7236.

How to cite this article: Perovich, D, Raphael, I, Moore, R, Clemens-Sewall, D, Lei, R, Sledd, A, Polashenski, C. 2023. Sea ice heat and mass balance measurements from four autonomous buoys during the MOSAiC drift campaign. *Elementa: Science of the Anthropocene* 11(1). DOI: <https://doi.org/10.1525/elementa.2023.00017>

Domain Editor-in-Chief: Jody W. Deming, University of Washington, Seattle, WA, USA

Guest Editor: Marcel Nicolaus, Alfred-Wegener-Institut Helmholtz-Zentrum für Polar- und Meeresforschung; Alfred-Wegener-Institut Helmholtz-Zentrum für Polar- und Meeresforschung, Bremerhaven, Germany

Knowledge Domain: Ocean Science

Part of an Elementa Special Feature: The Multidisciplinary Drifting Observatory for the Study of Arctic Climate (MOSAIC)

Published: November 29, 2023 **Accepted:** October 26, 2023 **Submitted:** January 10, 2023

Copyright: © 2023 The Author(s). This is an open-access article distributed under the terms of the Creative Commons Attribution 4.0 International License (CC-BY 4.0), which permits unrestricted use, distribution, and reproduction in any medium, provided the original author and source are credited. See <http://creativecommons.org/licenses/by/4.0/>.



Elem Sci Anth is a peer-reviewed open access journal published by University of California Press.

OPEN ACCESS 